remote sensing

MDPI

Article

Mapping Alpine Grassland Fraction Coverage Using Zhuhai-1 OHS Imagery in the Three River Headwaters Region, China

Fei Xing [1,2,3], Ru An [1], Xulin Guo [3], Xiaoji Shen [4,5,*], Irini Soubry [3], Benlin Wang [2,6], Yanmei Mu [3,7] and Xianglin Huang [2]

[1] College of Hydrology and Water Resources, Hohai University, Nanjing 210024, China; anrunj@hhu.edu.cn (R.A.)
[2] School of Earth Science and Engineering, Hohai University, Nanjing 211100, China
[3] Department of Geography and Planning, University of Saskatchewan, Saskatoon, SK S7N 5C8, Canada
[4] Yangtze Institute for Conservation and Development, Hohai University, Nanjing 210024, China
[5] Department of Civil Engineering, Monash University, Clayton, VIC 3800, Australia
[6] School of Geographic Information and Tourism, Chuzhou University, Chuzhou 239000, China
[7] Yanchi Research Station, School of Soil and Water Conservation, Beijing Forestry University, Beijing 100083, China
* Correspondence: xiaoji.shen@hhu.edu.cn

Abstract: The widely spread alpine grassland ecosystem in the Three River Headwaters Region (TRHR) plays an essential ecological role in carbon sequestration and soil and water conservation. In this study, we test the latest high spatial resolution hyperspectral (Zhuhai-1 OHS) remote sensing imagery to examine different alpine grassland coverage levels using Multiple Endmember Spectral Mixture Analysis (MESMA). Our results suggest that the 3-endmember (3-EM) MESMA model can provide the highest image pixel unmixing percentage, with a percentage exceeding 97% and 96% for pixel scale and landscape scale, respectively. The overall accuracy shows that Zhuhai-1 OHS imagery obtained the highest overall accuracy (83.7%, k = 0.77) in the landscape scale, but in the pixel scale, it is not as good as Landsat 8 OLI imagery. Overall, we can conclude that the hyperspectral imagery combined 3-EM MESMA model performs better in both pixel scale and landscape scale alpine grassland coverage mapping, while the multispectral imagery with the 3-EM MESMA model can satisfy requirements of alpine grassland coverage mapping at the pixel scale. The approaches and workflow to mapping alpine grassland in this study can help monitor alpine grassland degradation; not only in the Qinghai–Tibetan Plateau (QTP), but also in other grassland ecosystems.

Keywords: Zhuhai-1 OHS imagery; grassland fraction coverage; alpine grassland ecosystem; Three River Headwaters Region

Citation: Xing, F.; An, R.; Guo, X.; Shen, X.; Soubry, I.; Wang, B.; Mu, Y.; Huang, X. Mapping Alpine Grassland Fraction Coverage Using Zhuhai-1 OHS Imagery in the Three River Headwaters Region, China. *Remote Sens.* **2023**, *15*, 2289. https://doi.org/10.3390/rs15092289

Academic Editor: Yoshio Inoue

Received: 28 February 2023
Revised: 19 April 2023
Accepted: 25 April 2023
Published: 26 April 2023

1. Introduction

Grassland ecosystem is one of the most critical and widespread terrestrial ecosystems worldwide [1–3], covering 20–40% of the Earth's ice-free land surface [4–6]. The Qinghai–Tibetan Plateau (QTP) holds the largest alpine grassland ecosystem in the world [7,8], sheltering a rich diversity of flora and fauna [9]. However, research suggests that up to 90% of the grasslands on the QTP have been degraded [10] due to human activities and climate change [4,11,12]. Therefore, monitoring the status of QTP's grasslands, especially the alpine grasslands, under current global climate change is particularly important.

Traditionally, a grassland coverage assessment relies heavily on field investigation [13]; but field studies primarily focus more on small-scale areas and short-term periods, and are labor and time consuming and expensive; furthermore, due to the enormous spatial extent, remoteness, high elevation, and harsh environment on the QTP, it is inefficient for large-scale alpine grassland coverage mapping and monitoring [12]., Remote sensing techniques offer an effective and economical alternative approach for gathering spatial time-

series data for monitoring and mapping the alpine grassland coverage in this area [7,9,14,15].

Previous studies to map the alpine grassland coverage on the QTP have relied on coarse resolution and multispectral remote sensing data, to generate contextual information such as the Vegetation Index (VI) derived from MODIS and AVHRR-NDVI data. The study in [12] utilized the MODIS MCD 43A4 product to explore the grassland degradation on the Qinghai–Tibetan Plateau, and found that high spatial heterogeneity is better to indicate grassland degradation than that of low vegetation cover; another study [16] used every-10-day AVHRR-NDVI and every-10-day MODIS-NDVI data to assess the alpine grassland degradation index in Northern Tibet, and captured a very serious degradation situation in this area; the study in [17] use MODIS VI products (MOD13Q1) to model alpine grassland cover in the headwater region of the Huanghe River, and the result showed that MODIS NDVI data outperforms MODIS EVI data for modeling grassland cover in this area. These studies successfully obtained the appropriate result in grassland cover mapping; however, the coarse resolution and fee bands of these datasets (AVHRR-NDVI with a 8 km × 8 km spatial resolution, MCD43A4 with 500m, and MOD13Q1 with 250 m spatial resolution) can only provide a coarse resolution and general cover information in a very large scale (such as whole QTP), but are inferior in exploring more finer grassland cover in a more specific area.

Some image analysis techniques such as Linear Spectral Unmixing (LSU) and Spectral Angle Mapper (SAM) [7,18], and machine-learning techniques such as Random Forest Regression (RF), Support Vector Machine Regression (SVMR), and Partial Least Squares Regression (PLSR) have also been used to derive plant coverage from finer resolution remotely sensed images in previous studies and achieved high accuracy [19–21]. However, the results based on these methods were established on the use of extensive training samples [22] or the use of single hyperspectral and multispectral data; however, collecting adequate ground validation samples in the QTP area is unfeasible and multispectral data are unable to match the combined advantages of high-resolution and hyperspectral remote sensing data..

As an extension of the simple SMA (Spectral Mixture Analysis) approach, Multiple Endmember Spectral Mixture Analysis (MESMA) decomposes each pixel using different combinations of potential endmembers (model). This permits the number and types of endmembers to vary on a per-pixel basis, generating more reliable unmixing results for imageries with higher inter- and intra- endmember variance. In this way, the model with the lowest RMSE is selected to unmix each image pixel, resulting in the best fit across the entire image pixel [23–25], while there have been many studies that have monitored rangeland degradation in the Three River Headwaters Region (TRHR) [1,15,26]. However, few have used the MESMA method to investigate alpine grassland cover in the TRHR. Therefore, for reasons described, we proposed using the potential for the latest high-resolution hyperspectral data, Zhuhai-1 Orbita Hyperspectral (Zhuhai-1 OHS) imagery, analyzed using the MESMA method as a novel approach to large-scale TRHR monitoring.

The Zhuhai-1 OHS data have a swath width greater than 150 km and measuring 32 spectral bands at 10 m spatial and 2.5 nm spectral resolution, with the spectral wavelength ranging from 466 nm to 940 nm [27,28]. Due to its combined high spatial and spectral resolution, Zhuhai-1 OHS has been applied in a range of fields, including water resources monitoring [29], land cover mapping [27,30], vegetation monitoring [31], carbon sequestration monitoring [32], and soil moisture estimation [33], but has not been used in alpine grassland monitoring in the QTP region.

Therefore, the objective of this research is to investigate and evaluate the ability of the latest Zhuhai-1 OHS hyperspectral imagery in distinguishing the plant and non-plant at pixel scale, and mapping the alpine grassland fraction coverage at the landscape scale (i.e., high coverage, moderate coverage, and low coverage) level using the MESMA method in the TRHR.

2. Study Area

The TRHR (89°22′42″~102°14′10″E, 31°35′16″~36°15′31″N) lies in northwest China, the hinterland of the QTP (Figure 1), and is a critical ecological barrier of China. This region also refers to the source of the Yangtze River, Yellow River, and Lancang River, known as the "China Water Tower". The TRHR covers an area of approximately 358,000 km^2, with an average elevation of 4500 m above sea level. Due to the high altitude, the natural environmental conditions in TRHR are harsh, fragile, and sensitive to climate change [17], making it one of China's most important ecological function zones [34]. The climate of the TRHR is dominantly continental, the annual average temperatures ranging approximately from −6 °C to 4 °C, with significant diurnal temperature differences, and annual precipitation ranging from 260 mm to 780 mm which is highly variable in space and time. Approximately 80% of its annual precipitation falls from June to August, which is the peak of the growing season [15,17,35]. Our study area is located in the eastern TRHR (Figure 1), which is in the transition zone between the Animaqing Mountains and Zhaling–Eling Lake; two crucial ecozones in the Qinghai–Tibetan Plateau.

In the TRHR, grassland ecosystems occupy over 65% of the land area [15,36]. Aline grassland, comprised of the alpine steppe (Figure 2a) and alpine meadow (Figure 2b), is the main grasslands cover type in this region. Alpine meadows occupy most of the natural grassland in the TRHR (72.15%). Because of the high grass quality, and richness in grass nutrition, alpine meadows are excellent pastures with high utilization value in the TRHR [36–38]. The alpine steppe only accounts for 21.44% of the grassland area in this region [37–39]. Alpine grassland in this area not only plays a critical role due to the ecosystem services it provides for the TRHR, but it is also an essential resource that supplies over 90% of local residents' subsistence, such as grazing activities. Table 1 shows the dominant species, their distribution area, and the proportion of the alpine meadows and alpine steppe in the TRHR. Figure 2 shows the typical alpine grassland landscape in the TRHR.

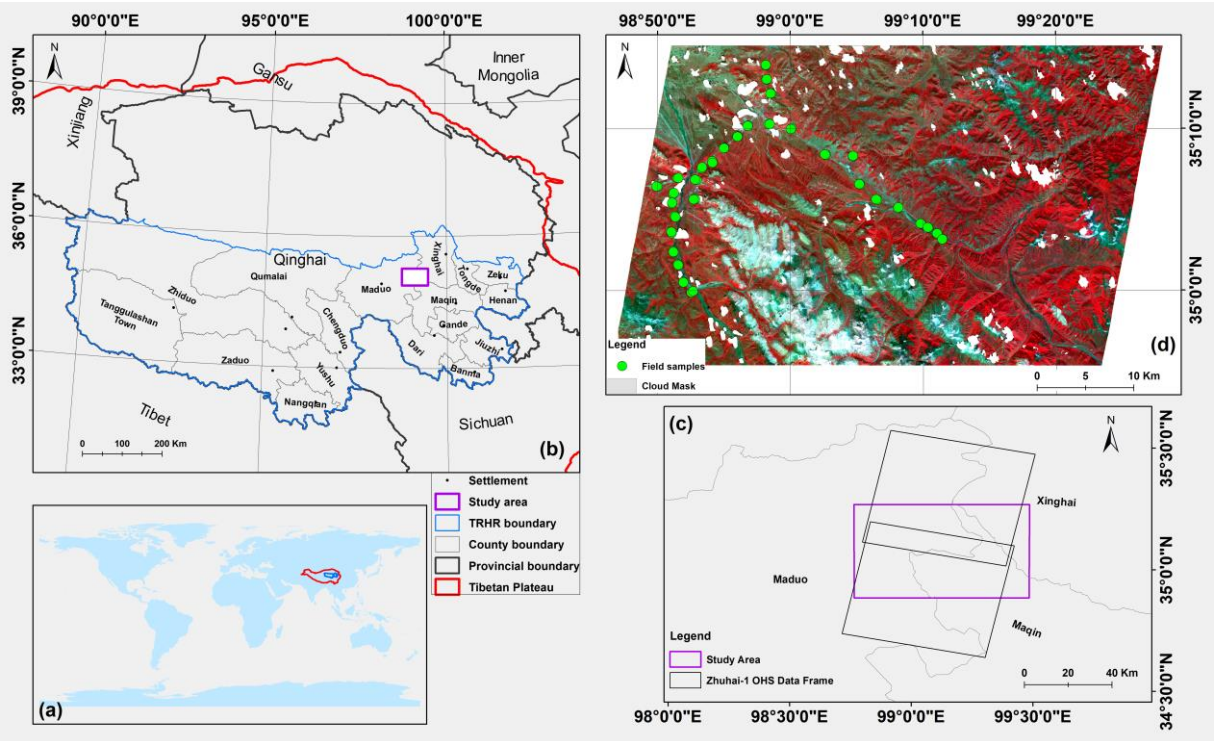

Figure 1. (**a**) Location of the TRHR at global scale, (**b**) location of the study area in the TRHR, (**c**) the Zhuhai-1 OHS imagery cover, and (**d**) locations of the sample sites and study area images of Zhuhai-1 OHS (b27: 866 nm, b13: 656 nm, b6: 550 nm). The Tibetan Plateau boundary comes from Zhang et al. (2021).

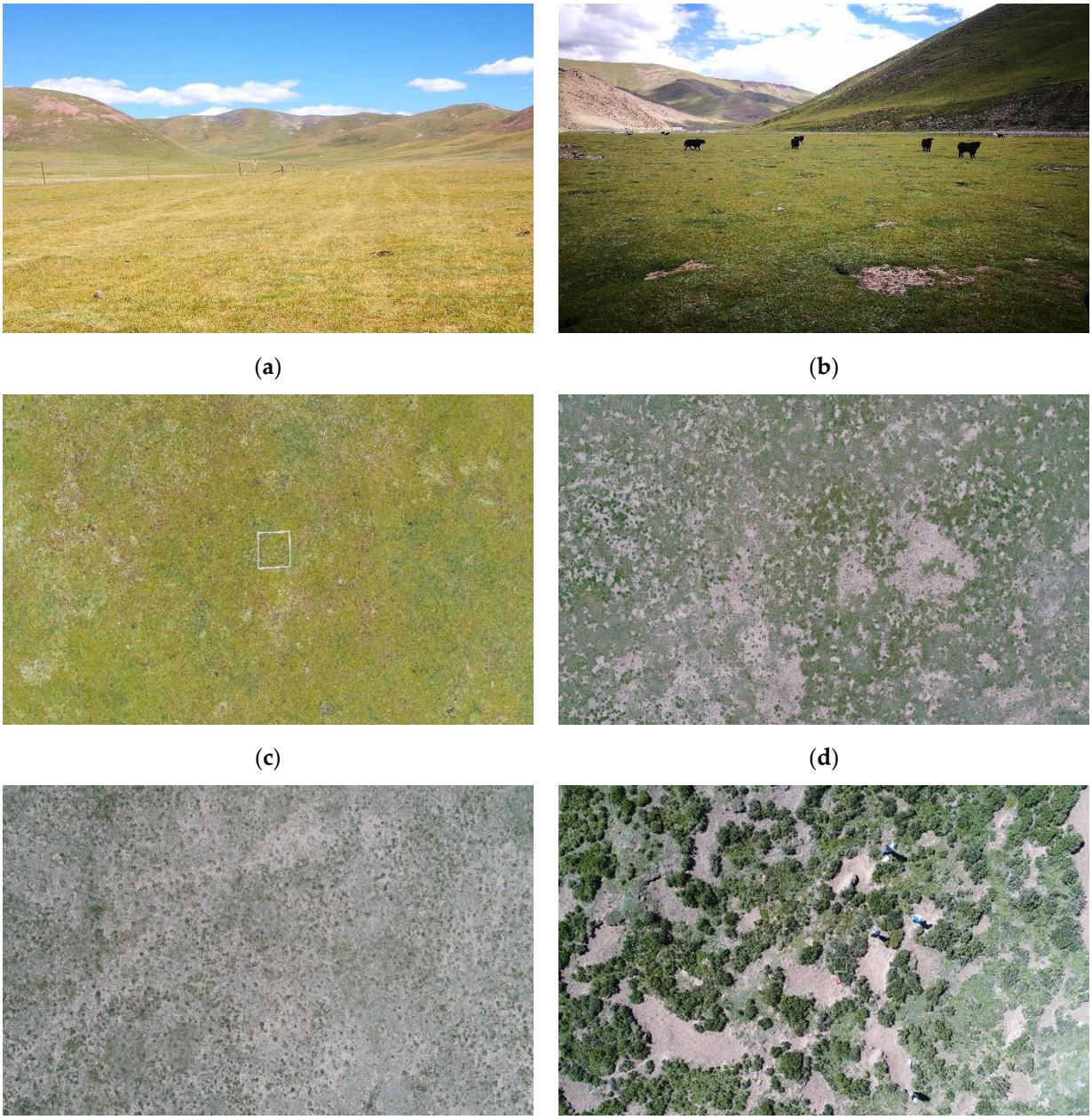

Figure 2. Photographs of the investigated alpine grasslands in the TRHR. (**a**) Picture of non-degraded grassland in southern Qumalai County in August 2019 showing a typical alpine steppe landscape. (**b**) Picture of a non-degraded alpine meadow in southeastern Zhiduo County in August 2019 showing an alpine meadow landscape, the animals in the picture are Yak, one of the most common grazing livestock of native Tibetan residents. (**c**) Picture of the high coverage alpine grassland in southern Qumalai County in August 2017. (**d**) Picture of the moderate coverage of alpine grassland. (**e**) Picture of the low coverage alpine grassland. (**f**) Picture of shrub cover in August 2017. All the pictures above were obtained by our research group. Picture (**a**,**b**) were taken by smartphone; (**c**–**f**) were taken by DJI Phantom 4 PRO; (**d**–**f**) were taken in northeastern Maduo County in August 2017.

Table 1. The dominant species, distribution area, and proportion of the alpine grassland in the TRHR.

Cover Type	Dominant Species	Co-Occurring Species	Distributed Area	Elevation (m)	Proportion	References
Alpine meadows	*Kobresia pygmaea*, *Kobresia humilis*, Kobresia capillifolia	*Herbarum variorum*, *Stipa aliena*, *Ptilagrostis* spp., and *Poa* spp.	Southwest, central south, and east part of the TRHR	3000~4800	72.15%	[37–40]
Alpine steppe	*Stipa purpurea*, *Carex moorcroftii*, *Brylkinia caudata*	*Herbarum variorum*, *Poa* spp., and *Leymus secalinus*	West and northwest of the TRHR	3800~4600	21.44%	

3. Materials and Methods

3.1. In-Situ Grassland Coverage Collection

A field survey was conducted between 2017 and 2019 during the peak growing season (mid-August). We set our sample plots in typical alpine grassland communities with homogeneous growth status. Previous studies have indicated correlations between settlements and plant coverage [41]. Therefore, all of our sample plots were set a minimum of 5 km far away from the settlement points to reduce the impact of human activities. In each investigated site, we set a 30 m by 30 m sample plot and kept at least a 100 m distance apart from each other to minimize the spatial autocorrelation between the sample plots [42–44]. For each sample plot, nine 1 m by 1 m independent subplots were set in four directions extending from the center of the sample plots (Figure S1). In addition, all the sample sites were at least 100 m away from roads and rivers to reduce their influence. Grassland type, dominant grass species, grassland coverage, and coordinates information with an accuracy of ~0.5 m, including latitude, longitude, and altitude, were collected in each subplot. The grassland coverage in each subplot was averaged to represent the sample plot's grassland coverage. In total, 63 sample plots were obtained in this study (Figure 1b).

In this study, we also collected in situ spectra to correct the spectra derived from satellite images by using the SVC-HR 512i Hand-Held spectrometer. The spectral reflectance value of this spectrometer ranges from 350–1075 nm and it has a spectral resolution of 3.5 nm with a minimum sampling interval of 1.5 nm. The in situ spectra were collected in each subplot in 1 m above the grass. In our study, all field-obtained grassland coverage and spectral reflectance data were used during the sample selection when employing the MESMA method.

3.2. Remote Sensing Imagery Acquisition and Data Processing

The Zhuhai-1 OHS imagery used in this study was acquired on 19 August 2020, and downloaded at Level-1B processing from the Data Express website (Orbita). The data preprocessing included layer stacking, radiometric calibration, and rational polynomial coefficient orthorectification [45]. The geometric correction was conducted using the processed Sentinel-2A images as the reference data, resulting in an error of fewer than 0.5 pixels. In addition, because the Zhuhai-1 OHS imagery was acquired with a thin slump cloud, we manually digitized the cloud and then masked the cloud area to reduce its influence. We did not use a cloud masking algorithm since our study region is small and manually masking the cloud can obtain higher accuracy [9]. Moreover, due to the high elevation and great terrain relief of our study region, the VECA (Variable Empirical Coefficient Algorithm) [46–48] topographic correction model was applied to all three satellite imageries. After the above processing, all images were clipped to the study area boundary. Furthermore, the commonly used Sentinel-2 and Landsat 8 OLI imagery was also used in this study to compare the ability of grassland fraction coverage mapping. Table 2 shows the detailed information of the remote sensing imagery in our study.

Table 2. Remote sensing imagery used in our study.

Data Sources	Acquisition Date	Bands	Spatial Resolution (m)	Spectral Resolution (nm)	Wavelength Region (nm)	Scenes
Landsat 8 OLI	25 August 2020	7	30	/	450~880, 1570~2290	2
Sentinel-2	17 September 2020	13	10	/	443~945, 1610~2190	4
Zhuhai-1 OHS	19 August 2020	32	10	2.5	400~1000	2

3.3. Land Use/Cover Datasets

Our study used two Land Use/Cover datasets as reference data (Table 3). The first one is the China's National Land Use and Cover Change (CNLUCC) dataset (Table 3) with 30 m spatial resolution which was developed by [49]. The overall accuracy is reported to be higher than 90%, and the latest 2020 dataset was used in our study. The dataset was provided by the Data Center for Resources and Environmental Sciences, Chinese Academy of Sciences (RESDC) (http://www.resdc.cn (accessed on 20 July 2022)) [49]. We resampled the data to 10 m spatial resolution to match the spatial resolution of remote sensing imagery used in the study, and extracted the grassland layer from the dataset as the reference data. The second one is the 10 m spatial resolution global-scale land cover dataset: ESA WorldCover 10 m 2020 v100 (ESA WorldCover) [50] (Table 3). The overall accuracy of this dataset is 74.4 ± 0.1% for 2020 on a global scale, with the highest accuracy of 80.7% for Asia. In terms of land cover types, tree cover and snow/ice, cropland, water body, and bare/sparse vegetation classes had high accuracies, while shrubs, herbaceous wetland, and moss/lichen classes were mapped with lower accuracies [51]. The selected land cover types such as tree cover, shrubland, grassland, moss, and lichen from the ESA World Cover dataset were merged into plants, and the left land cover types were merged into non-plants. The selected high-density grassland, medium-density grassland, and low-density grassland layers from the CNLUCC datasets were used to assess the accuracy of the sub-coverage level unmixing results.

Table 3. Description of the two land use/cover datasets.

Data Source	Spatial Resolution (m)	Year	Land Cover Types
CNLUCC	30	2020	Cultivated, forest, grassland (high-density grassland, medium-density grassland, low-density grassland), water, construction, and unused land
ESA WorldCover	10	2020	Tree cover, shrubland, grassland, cropland, built-up, bare/sparse vegetation, snow and ice, permanent water bodies, herbaceous wetland, mangroves, moss, and lichen

3.4. MESMA Method Procedure

Following previous studies [24,52,53], georeferenced polygons with metadata from the field survey data and FROM-GLC10 were used to define the potential endmembers of the land cover types included in our study area. The polygons with metadata were created with the open-source add-on software Visualization and Image Processing for Environmental Research (VIPER) Tools (v2.1) [54]. We selected the polygon samples in the Zhuhai-1 OHS, Landsat 8, and Sentinel-2 images, respectively. Then, we generated three potential spectral libraries with the polygons obtained from the endmembers of the three images.

To form the optimized spectral libraries, we used three techniques that have been used in previous studies: (1) Endmember Average RMSE (root mean squared error) (EAR), which selects the endmembers that yield the minimum RMSE within a class [55]; (2) Count-based Endmember Selection (CoB), which determines the number of spectra modeled by an endmember within their class (InCoB) and outside their class (OutCoB); and (3) Minimum Average Spectral Angle (MASA), which selects the endmembers

considering the minimum average spectral angle criterion between each candidate endmember [56]. We followed the approach suggested by Roberts [54], and we selected the optimized endmembers for each ground component by firstly using the lowest EAR, then by the highest InCoB, and finally the highest MASA value.

Once the final optimal spectral libraries were built and the selected endmembers were identified, we regrouped the endmembers in two ways. The first one was at the pixel scale, similar to the previous works [52,57]. These levels were organized into green vegetation (GV), non-photosynthetic vegetation and soils (NPVS), and shade. The second one was at the landscape scale, where we regrouped the endmembers to: low coverage grassland (LCG), moderate coverage grassland (MCG), high coverage grassland (HCG), and others (Oth). In this study, we enable different model complexities for each pixel to be unmixed and use multi-level model complexity combinations as used in [52,57]. In this study, we used a partially-constrained mode when conducting MESMA with the following model selection criteria: 0 and 1 were defined as the minimum and maximum allowable fraction values; 0 and 0.8 were set as the minimum and maximum permissible shade fraction values, and 0.025 was defined as the maximum allowable RMSE. In the case where several models fit these criteria, the model with the lowest overall RMSE was selected. Furthermore, we defined 95% of a pixel as the lowest acceptance threshold for an unmixing process. If the condition was unfulfilled, we repeated the unmixing process by adjusting the endmember type and/or the number of the ground component spectra included in the spectral libraries. Shade normalization was applied to the unmixed fraction images to remove the contribution of the shade endmembers and to obtain more relative abundance information of the non-shade endmembers [54].

3.5. Accuracy Assessment

The accuracy of the MESMA classification results was assessed by calculating a confusion matrix that used independent validation samples. The validation samples in this study are pixel-based firstly, the sample polygons were converted to points by using their center point, then the point was converted to raster pixels, and the overlapping of the classified pixel, the referenced land use pixel, and the sample pixel were considered corrected classified.

Following [58] and [53,59,60], the Overall Accuracy (OA), Producer's Accuracy (PA) (omission errors), User's Accuracy (commission errors), and Kappa (K) statistics were calculated. In addition, similar to Clark [61] and Quintano [52], Z statistics were computed from K statistics and variance to compare the accuracy of the acquired unmixed grassland coverages from each input data source. At the 95% confidence level, only $Z \geq 1.96$ is considered significant [58,62].

3.6. RMSE Distribution Analysis

We also analyzed the relationship between RMSE variations and topographic attributes during the MESMA unmixing process. We divided the elevation by a 100 m gradient from 3500 m to 5200 m in the study area. The aspect was divided into nine groups as follows: <−1: flat; 0–22.5° and 337.5°–360°: north; 22.5°–67.5°: northeast; 67.5°–112.5°: east; 112.5°–157.5°: southeast; 157.5°–202.5°: south; 202.5°–247.5°: southwest; 247.5°–292.5°: west; 292.5°–337.5°: northwest. The slope was divided by 10% gradients to indicate the topographical relief. Version 3 of the Advanced Spaceborne Thermal Emission and Reflection Radiometer (ASTER) Global Digital Elevation Model (DEM) (ASTER GDEM V3) dataset used in this study was obtained from Geospatial Data Cloud (GDC, http://www.gscloud.cn (accessed on 10 December 2019)) at 30 m spatial resolution, and clipped to the study area boundary.

4. Results

4.1. MESMA Classification

At the pixel scale, the mean image pixel percentages of MESMA unmixed for the Zhuhai-1 OHS images were 98.5% and 99.1% with the 2-EM and 3-EM models, respectively; and for the landscape scale, the percentages with the 2-EM, 3-EM, and 4-EM models were 96.3%, 99.1%, and 98.6%, respectively. Furthermore, there are significant differences between the 2-EM and 3-EM results at the pixel scale ($p < 0.001$), and among the 2-EM, 3-EM, and 4-EM results at the landscape scale ($p < 0.001$). In particular, the 3-EM model results in the highest value of pixels classified for both the pixel scale, and landscape scale. Table 4 includes the details of the unmixing results for the three images under different model complexities.

At the pixel scale, the pixel unmixing percentage obtained from the Zhuhai-1 OHS imagery was lower than that from the Landsat 8 OLI imagery but higher than that of the Zhuhai-1 OHS imagery with the 2-EM models (Table 4); while when using the 3-EM models, the Zhuhai-1 OHS imagery got the highest unmixed percentage (Table 4). At the landscape scale, the pixel unmixed percentage obtained from the Zhuhai-1 OHS imagery is higher than that from both the Landsat 8 OLI and Sentinel-2 imagery with the 3-EM and 4-EM models, but the pixel unmixed percentage obtained from Zhuhai-1 OHS imagery with the 2-EM models showed the same trend at the pixel scale. Therefore, based on our results and previous studies [63,64], we used the 3-EM model unmixed fractions' results in the next analysis.

Table 4. Summary of MESMA unmixing results.

Model Complexity	Landsat 8 OLI	Sentinel-2	Zhuhai-1 OHS
Number of pixels classified and the overall percentage (%) classified in each image at pixel scale			
2-EM	98.9	97.2	98.5
	8,995,210	19,888,207	19,501,999
3-EM	98.5	97.5	99.1
	8,960,561	19,946,983	19,613,810
Number of pixels classified and the overall percentage (%) classified in each image at landscape scale			
2-EM models	97.6	95.1	96.3
	8,870,491	19,469,101	19,066,003
3-EM models	98.5	96.6	99.1
	8,954,389	19,762,221	19,611,130
4-EM models	95.6	94.3	98.6
	8,696,568	19,302,190	19,520,686

Notes: EM: endmember.

Figures 3 and 4 show the shade-normalized fraction images derived from the Landsat 8 OLI, Sentinel-2, and Zhuhai-1 OHS images by MESMA with the 3-EM models in pixel scale, and landscape scale, respectively. Regardless of the GV fraction or NPVO fraction, the fractions obtained from the Landsat 8 OLI imagery had a stronger contrast with the background, followed by the results from the Sentinel-2 imagery; the fraction results obtained from the Zhuhai-1 OHS imagery had the lowest contrast.

From Figure 4, we can see that the HCG fractions derived from Landsat 8 OLI imagery (Figure 4(a1)) cover the largest area, followed by the results obtained from Sentinel-2 imagery (Figure 4(a2)) and Zhuhai-1 OHS imagery (Figure 4(a3)). The MCG and LCG fraction results (Figure 4(b1–b3,c1–c3)) show the opposite trend. When looking at the Others fraction results (Figure 4(d1–d3)), the Landsat 8 OLI and Sentinel-2 images show a higher abundance than that of the Zhuhai-1 OHS imagery.

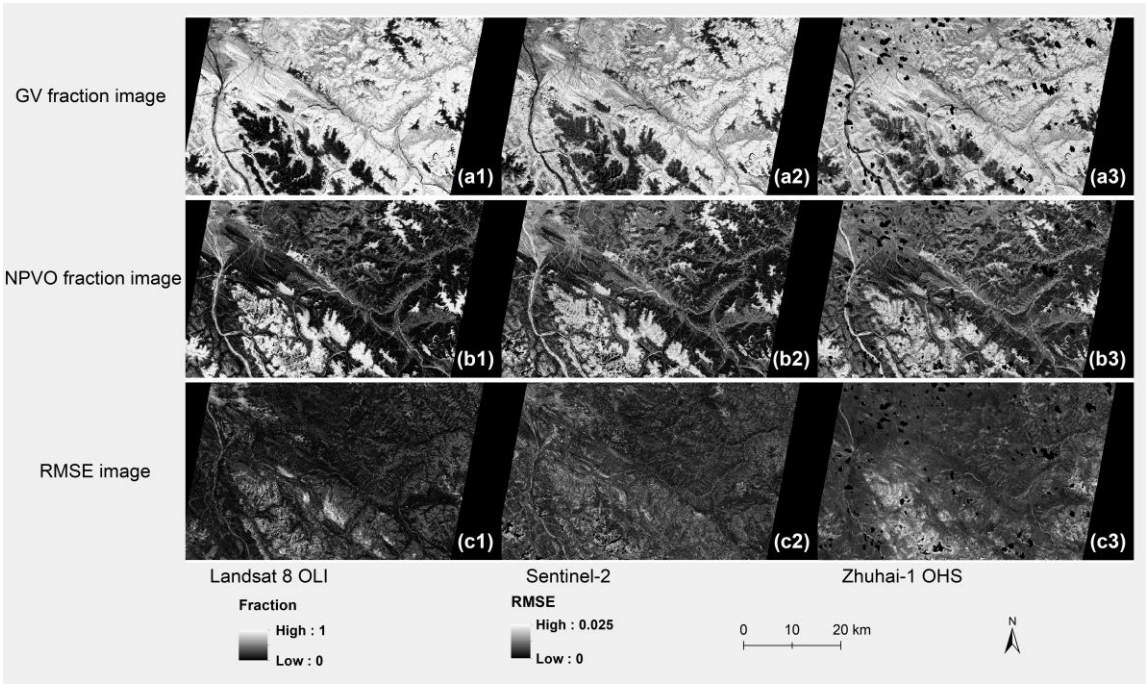

Figure 3. Shade-normalized fraction images for pixel scale coverage. (**a1–a3**) GV fraction image derived from Landsat 8 OLI, Sentinel-2, Zhuhai-1 OHS images, respectively; (**b1–b3**) NPVO fraction image derived from Landsat 8 OLI, Sentinel-2, Zhuhai-1 OHS images, respectively; (**c1–c3**) RMSE distribution images for Landsat 8 OLI, Sentinel-2, Zhuhai-1 OHS images, respectively.

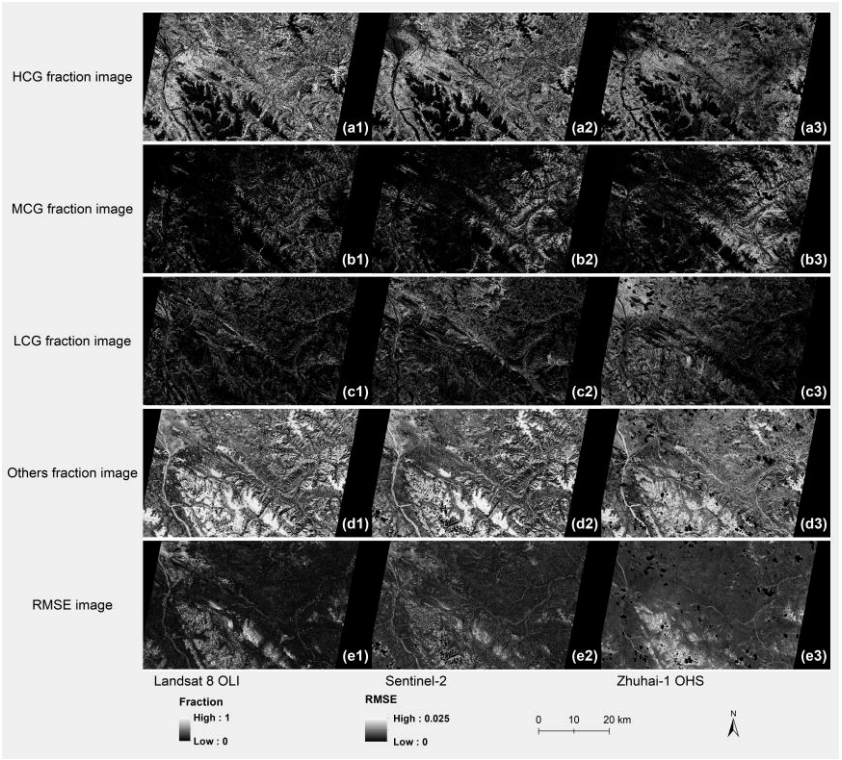

Figure 4. Shade-normalized fraction images for landscape scale. (**a1–a3**): HCG fraction images derived from Landsat 8 OLI, Sentinel-2, Zhuhai-1 OHS images, respectively; (**b1–b3**): MCG fraction images derived from Landsat 8 OLI, Sentinel-2, Zhuhai-1 OHS images, respectively; (**c1–c3**): LCG fraction images derived from Landsat 8 OLI, Sentinel-2, Zhuhai-1 OHS images, respectively; (**d1–d3**): Others fraction images derived from Landsat 8 OLI, Sentinel-2, Zhuhai-1 OHS images, respectively; (**e1–e3**): RMSE distribution images for Landsat 8 OLI, Sentinel-2, Zhuhai-1 OHS images, respectively.

From visual inspection, at the pixel scale, we can see that the Zhuhai-1 OHS, Landsat 8 OLI, and Sentinel-2 imagery all have the ability to discriminate the vegetated and non-vegetated areas, and we can clearly distinguish the built-up, riverbed, and road area in the unmixing fraction (Figure 5(a1–a3)). Meanwhile, within the same land cover classes (GV or NPVO), the objects were more clustered in the unmixed results of the Landsat 8 OLI and Sentinel-2 imagery than in the Zhuhai-1 OHS imagery (Figure 5(a3)). However, at the landscape scale, the results derived from the Zhuhai-1 OHS imagery performed better in presenting detailed information on grassland coverage than that from Landsat 8 OLI and Sentinel-2 imagery (Figure 5(b1–b3)) and (Figure S2(c1–c3,d1–d3)).

Spatially, we can see the high value-zone of the RMSE fraction for all three image sources was clustered and distributed in the mountain area with high altitudes (Figure S3) and steep slopes (Figure S4). Especially, the result from the Landsat 8 OLI imagery (Figure 3(c1)) is the most obvious, and followed by the Landsat 8 OLI imagery, while the RMSE result from the Zhuhai-1 OHS imagery (Figure 3(c3)) is more dispersed. Statistically, we can see from Figure 6 that for all the three image sources, the RMSE value was rising with the elevation and slope growth, but there are no obvious RMSE variations between the aspect changes (Figure S5). As for the different data sources, the Zhuhai-1 OHS imagery obtained the highest RMSE result during the unmixing process, followed by the Sentinel-2 imagery; the RMSE result obtained from the Landsat 8 OLI imagery was kept at a low level.

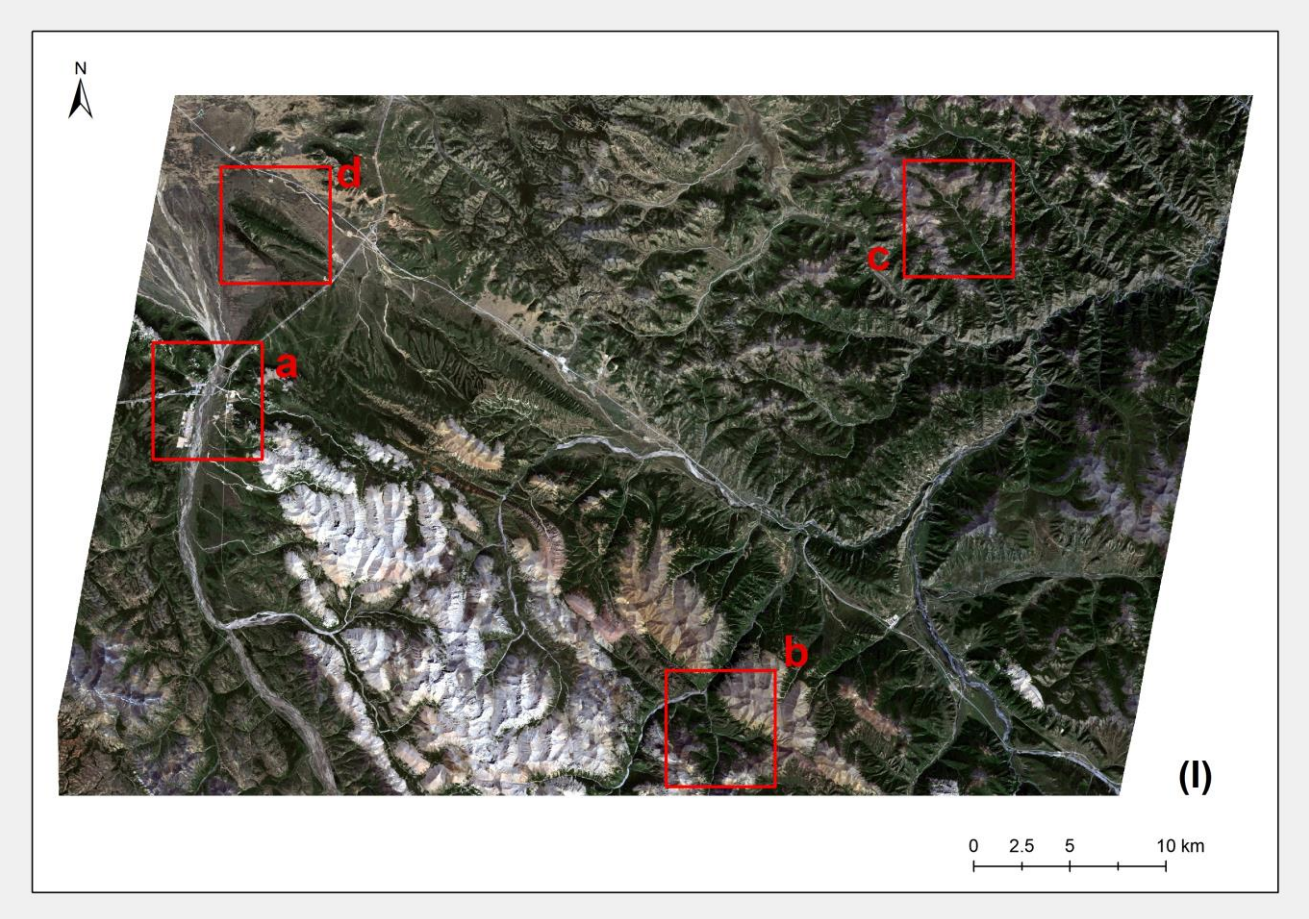

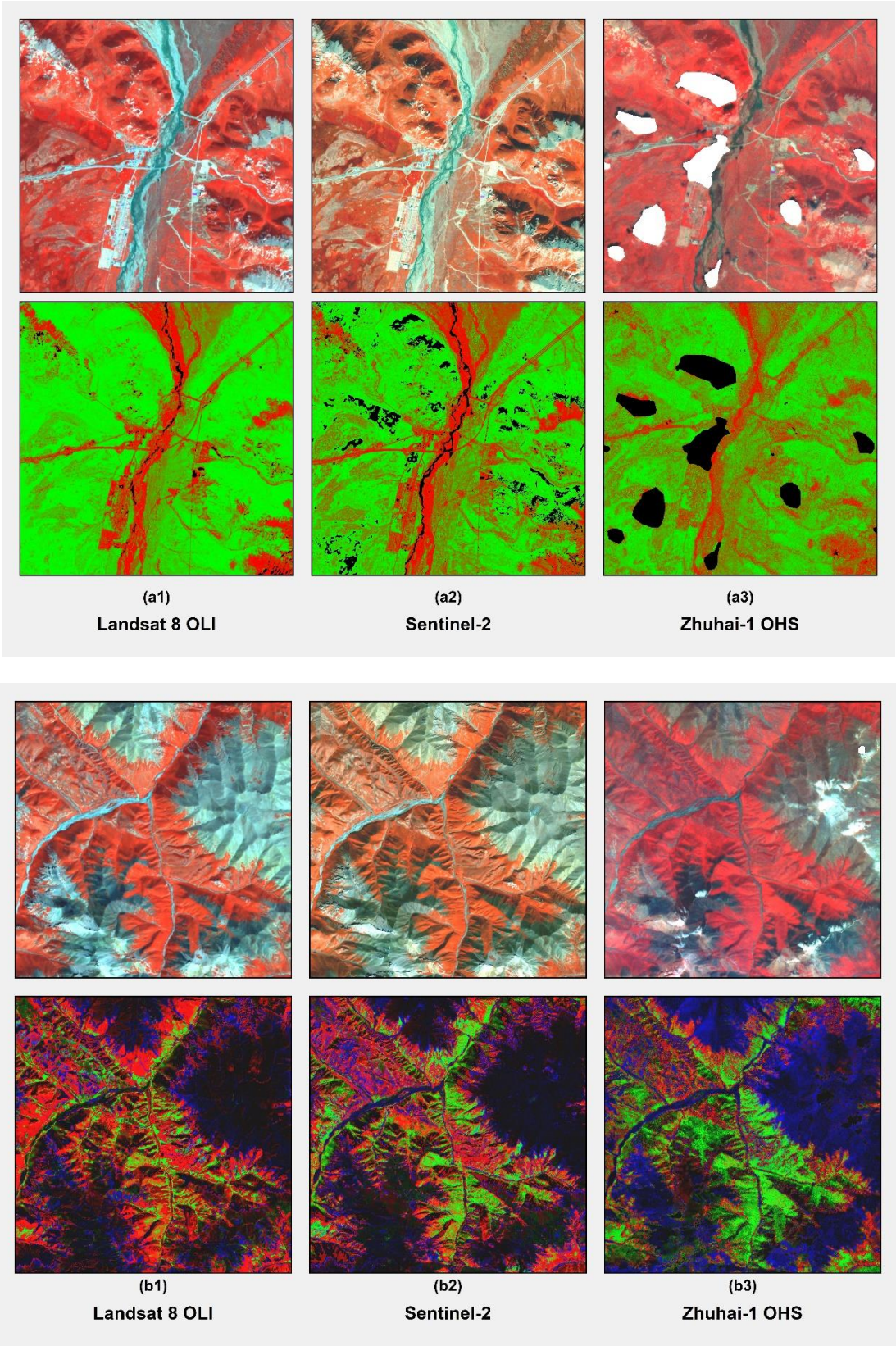

Figure 5. Comparison of unmixed results derived from the Landsat 8 OLI, Sentinel-2, and Zhuhai-1 OHS images. (**I**) Full study area scene that includes subsequent comparison locations. (**a1**–**a3**) Zoomed in view of point (**a**). (Top row are original images, and bottom row are unmixed results of different image sources) for pixel scale results. Green represents the GV fraction, red represents the NPVO fraction, and the black proportion represents the image pixels that were not unmixed. (**b1**–

b3) Zoomed in view of point (**b**) for landscape scale results. Red represents HCG fractions, green represents MCG fractions, and blue represents LCG fractions. The black parts in the Zhuhai-1 OHS imagery were cloud masked. For the detailed information for point (**c**) and point (**d**), please see Figure S2.

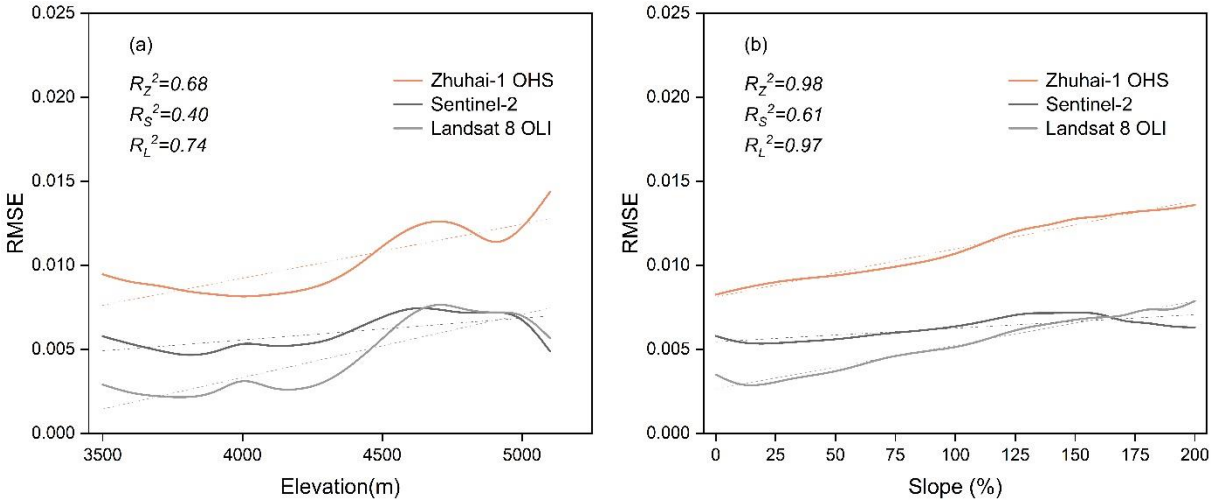

Figure 6. Distribution of RMSE observed from various (**a**) elevations and (**b**) slope for the three image sources. R_Z^2, R_S^2, and R_L^2 are the R2 for the Zhuhai-1 OHS, Sentinel-2, and Landsat 8 OLI imagery, respectively.

4.2. Endmember Spectral Libraries

The georeferenced polygons from the fieldwork reference and the land use map assisted us in finding the most suitable spectra of each land cover class in our study area. Figure 7 provides an example of the selected endmember spectra for each category in the three image sources. In Figure 7, we can see that in GV spectral libraries, the reflectance of ground objects that appear in the Zhuhai-1 OHS imagery is higher than that of the Landsat 8 OLI and Sentinel-2 imagery; especially GV1 and GV2 (Figure 7c). For Landsat 8 and Sentinel-2 imagery, the ability to discriminate detailed GV objects can extend from 875 nm (NIR) bands to 2235 nm (SWIR) bands, while the Zhuhai-1 OHS imagery can only provide a short spectral range, even though with more spectral bands than the Landsat 8 OLI and Sentinel-2 imagery. The shortage in band wavelength limited the discriminate ability of the objects in the Zhuhai-1 OHS imagery. The NPVO ground objects showed a clustered trend in all three imageries, and this phenomenon provided a good chance to distinguish them from the GV objects, particularly in the Sentinel-2 imagery. At the landscape scale, Zhuhai-1 OHS showed the best ability to distinguish the grassland and other objects for wavelengths from 490 nm to 700 nm, LCG, HCG, and MCG in wavelengths from 800 nm to 900 nm, and it can capture the small differences between HCG and MCG in wavelengths from 825 nm to 875 nm. This demonstrates the advantages of the high spectral resolution of Zhuhai-1 OHS imagery, and it shows the ability of the hyperspectral data to discriminate the ground objects even in short wavelengths.

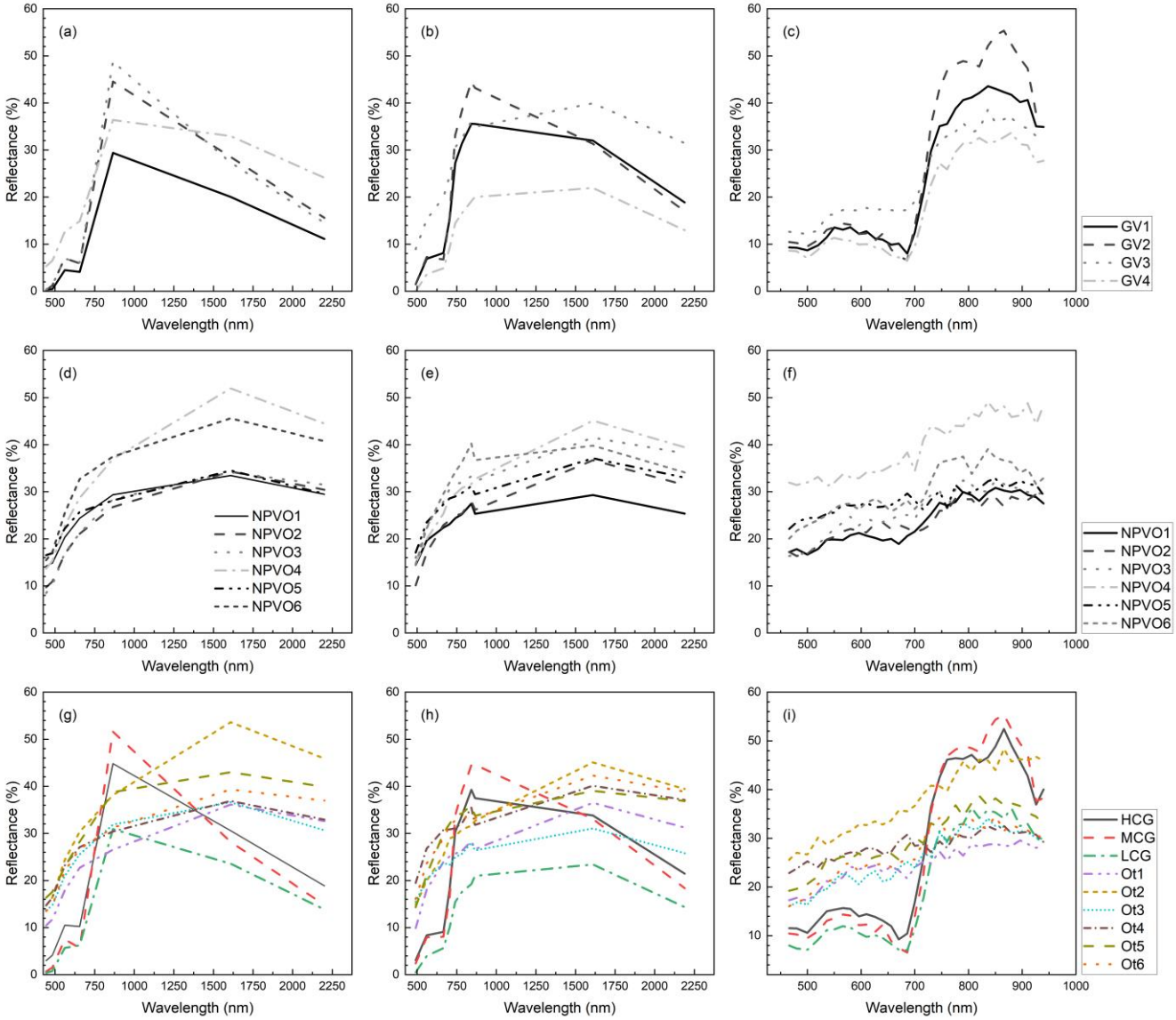

Figure 7. Example endmember spectra from the final optimized spectral libraries. (**a**–**c**) Green vegetation spectral libraries at the pixel scale coverage from Landsat 8 OLI, Sentinel-2, and Zhuhai-1 OHS images, respectively; (**d**–**f**) Non-photosynthetic vegetation and other components spectral libraries at the pixel scale coverage from Landsat 8 OLI, Sentinel-2, and Zhuhai-1 OHS images, respectively; (**g**–**i**) HCG, MCG, LCG and Others spectral libraries at the landscape scale from Landsat 8 OLI, Sentinel-2, and Zhuhai-1 OHS images, respectively.

4.3. MESMA Classification Accuracy

At the pixel scale (Table 5), the OA was 91.1%, 88.0%, and 92.3% for Landsat 8 OLI, Sentinel-2, and Zhuhai-1 OHS images, respectively. The highest PA (96.9%, 98.0%) and UA (99.4%, 89.8%) for the GV and NPVO fractions were both obtained from the Landsat 8 OLI imagery, respectively. The Sentinel-2 image provided the lowest PA (96.7%, 92.1%) and UA (97.8%, 88.6%) for both GV and NPVO fractions. A significance test of the k-statistic values for each image source ($Z = 41.45$, 32.05, and 39.12 respectively, all >1.96) indicates that using all of the three images to estimate the plant cover with MESMA classification can be utilized to make a plant coverage map with a 95% confidence level. The Z-test of the MESMA classification ($Z = 0.41$, 0.41, and 0.86, respectively, all <1.96) showed that there is no significant statistical difference among three images.

Table 5. The accuracy parameters for MESMA classification with 3-EM Landsat 8 OLI, Sentinel-2, and Zhuhai-1 OHS. Images' results at the pixel scale.

Accuracy Parameters	Landsat 8 OLI		Sentinel-2		Zhuhai-1 OHS	
	GV	NPVO	GV	NPVO	GV	NPVO
PA (%)	91.1	90.9	85.5	96.8	92.1	93.1
UA (%)	97.3	73.8	99.0	65.0	98.0	76.6
OA (%)	91.1		88.0		92.3	
k-statistic	0.76		0.70		0.79	
Z_k-statistic	20.8		17.9		23.6	
$Z_{L8\text{-}S2}$-statistic	0.7					
$Z_{L8\text{-}ZOHS}$-statistic	0.7					
$Z_{S2\text{-}ZOHS}$-statistic	1.86					

Notes: PA: producer's accuracy; UA: user's accuracy; OA: overall accuracy; GV: green vegetation; NPVO: non-photosynthetic vegetation and other components in the study area. s for each data source was to confirm that wheatear the classification based on these data sources is meaningful, and the Z-statistic between each data source was to reveal that wheatear the classification between each two data sources is significantly different from each other.

Regarding the landscape scale (Table 6), the OA was 78.9%, 76.2%, and 83.7% for the Landsat 8 OLI, Sentinel-2, and Zhuhai-1 OHS images respectively, lower than that of the pixel scale coverage for all image sources. The highest PA for HCG (79.3%) and LCG (60.3%) were obtained from the Landsat 8 OLI and Sentinel-2 imagery, respectively; the highest PA for MCG (100 %) and Others (95.2%) were both derived from the Zhuhai-1 OHS imagery, respectively. The highest UA for HCG (75.0%) and MCG (80.0%) were obtained from the Sentinel-2 and Landsat 8 OLI imagery, respectively; and the highest UA for LCG (95.0%) and Others (90.9%) were both derived from the Zhuhai-1 OHS imagery, respectively. The Others acquired the highest PA and UA both internally for each image source and across image types, followed by MCG, and HCG with a moderate PA and UA. The Z-test showed that all the three classification results were statistically significant at a 95% confidence level ($Z = 19.1, 20.3, 26.6 > 1.96$). The Z-test value between each two image sources' k-statistic revealed no statistical differences for the MESMA classification results derived from the Landsat 8 OLI imagery and Sentinel-2 imagery ($Z = 0.1 < 1.96$). However, the classification results showed significant statistical differences between either the Zhuhai-1 OHS imagery and Landsat 8 OLI imagery ($Z = 2.4 > 1.96$), or the Zhuhai-1 OHS imagery and Sentinel-2 imagery ($Z = 2.3 > 1.96$).

Table 6. Summary of accuracy parameters for MESMA classification with 3-EM model complexity Landsat 8 OLI, Sentinel-2, and Zhuhai-1 OHS images' results at the landscape scale.

Accuracy Parameters	Landsat 8 OLI				Sentinel-2				Zhuhai-1 OHS			
	HCG	MCG	LCG	Others	HCG	MCG	LCG	Others	HCG	MCG	LCG	Others
PA (%)	69.5	68.8	43.8	79.4	60.9	76.4	55.6	80.8	60.8	92.0	54.4	88.4
UA (%)	54.0	70.7	55.3	83.3	70.0	63.2	59.3	82.5	63.3	76.2	78.7	84.3
OA (%)	68.7				70.0				77.4			
k-statistic	0.57				0.60				0.69			
Z_k-test	15.3				16.8				21.1			
$Z_{L8\text{-}S2}$-statistic	0.5											
$Z_{L8\text{-}ZOHS}$-statistic	2.4											
$Z_{S2\text{-}ZOHS}$-statistic	1.92.3											

Notes: PA: producer's accuracy; UA: user's accuracy; OA: overall accuracy; HCG: high coverage grassland; MCG: moderate coverage grassland; LCG: low coverage grassland; Others: dry and dead grass, river band, and other non-plant components in our study area. Zk-statistic for each data source was to confirm that wheatear the classification based on these data sources is meaningful,

and the Z-statistic between each data source was to reveal that wheatear the classification between each two data sources is significantly different from each other.

5. Discussion

5.1. MESMA Endmember Selection and Model Performance

Both at the pixel scale, and landscape scale, with either the 2-EM, 3-EM, or 4-EM models, the mean percentage of the image pixels classified by MESMA using Landsat 8 OLI, Sentinel-2, and Zhuhai-1 OHS images exceeded 95% with an RMSE value smaller than 0.025. More specifically, this percentage exceeded 98% for the 3-EM models. One of the main reasons for this high percentage of unmixed pixels was the appropriate candidate endmember selection approach used to construct the spectral library. As a previous study mentioned, the successful application of linear pixel unmixing must satisfy several conditions for the selected endmembers, such as the linear independency of the spectra, their representativeness, and approximate constant-ness over the scene, their high number, and their identifiability [65]. Furthermore, the way in which the endmembers were organized, such as in GV, NPV, and other components of the study area used by [52,66] in their studies to identify forest burn severity in the Mediterranean region obtained a pixel unmixing percentage overall 99%. Consequently, the accurate pixel scale coverage and landscape scale for the alpine grassland ecosystem were acquired from the fraction images.

Although the results indicate that both the Landsat 8 OLI, Sentinel-2, and Zhuhai-1 OHS images have an excellent performance (mean percentage of image pixel classified exceeding 95%) in the unmixing procedure, there were differences in the ability to discriminate the grassland coverages. Similar results are also mentioned in the previous studies [63,64], where obtaining a high pixel unmixing percentage, the classification accuracy can be low as well. All this indicates that in the simple land surface cover unmixing cases (e.g., GV, NPVO, and shade), multispectral imagery combined with the appropriate model complexity (3-EM) can obtain almost the same high-performance unmixing result as hyperspectral imagery (Table 4). Moreover, we saw that hyperspectral imagery can even achieve a lower unmixed percentage (2-EM) than multispectral imagery (Table 4). One of the possible reasons for this could lay in the simple landcover combinations. Hyperspectral imagery provides a high number of spectral bands (Zhuhai-1 OHS provided 32 bands) and could cause much easier spectral confusion between objects, which would not exist in multispectral imagery's classic spectral band combinations. Nevertheless, in more complex land cover unmixing (e.g., HCG, MCG, LCG, Others, and shade), the high number of spectral bands provided by the hyperspectral imagery allows for more sensitivity to the specific unmixing objective, and performs better than the multispectral imagery (Table 4). Furthermore, we found that a more complex model does not necessarily lead to better unmixed results. Previous studies have suggested that natural and disturbed systems are best modeled by two or three models [64,67–69]. Hence, a higher model complexity should only be selected when the error decrease related to complexity exceeds a specific threshold [70,71].

At the pixel scale, the overall accuracy for all three image sources exceeded 95%. While at the landscape scale, the overall accuracy for all three image sources was above 75%. Thus, the overall accuracy for all three image sources decreased compared to that at the pixel scale. The overall accuracy of the Sentinel-2 imagery had the most significant decline, dropping by 19.5%, followed by the Landsat 8 OLI imagery, which decreased by 18.3%. The Zhuhai-1 OHS imagery had the lowest decline, which was only 13.0%. All this demonstrates the differences in the ability to model the details of land cover types between multispectral and hyperspectral images. At the pixel scale, we only grouped the endmembers into two types; therefore, the endmembers are more clustered within one type. When we regroup the endmembers into four categories at the landscape scale, the lower number of spectral bands provided by multispectral imagery may not be able to discriminate the minor differences between the different categories. In contrast, the hyperspectral imagery

with more spectral bands can provide more sensitivity in distinguishing the minor differences between the different categories.

When we compare the producer's and user's accuracy of different categories at the landscape scale; we find that low coverage grassland obtained the lowest producer's accuracy in all three image sources, and a relatively lower user's accuracy in the Landsat 8 OLI imagery as well. This agrees with the studies of [63,72,73] who observed a lower accuracy for low coverage land cover types. According to our field survey and prior knowledge about the research area, one of the main reasons for low classification accuracy in the low coverage alpine grassland region is that, in this region, there is a large proportion of bare land coverage, causing the soil background to have a stronger effect than the low coverage alpine grassland within one image pixel. This made the low coverage grassland spectra weak and influenced by bare ground (Figure 2e). On the other hand, the few spectral bands provided by the multispectral imagery are also one of the reasons, combined with its low spectral resolution which highlighted the shortcomings. For the hyperspectral imagery used in our study, although the Zhuhai-1 OHS imagery provided more spectral bands (32 bands) and a higher spectral resolution (2.5 nm), the spectrum scope only ranged from 466 nm to 940 nm, and there was no spectral information provided in the shortwave region. As for the spatial resolution, the 15 m, 10 m, and 10 m spatial resolution of the Landsat 8 OLI, Sentinel-2, and Zhuhai-1 OHS imagery, respectively, may not have the capability to capture a small patch of the low coverage alpine grassland which has a fragmented distribution over the region.

In addition, the spatial distribution of the results with the Landsat 8 OLI imagery and Sentinel-2 imagery showed a concentrated pattern; the same class is always present as a large patch, showing a sudden transition and clear boundary between different coverage levels, while the results derived from the Zhuhai-1 OHS imagery showed a staggering spatial distribution; the transitions between different coverage levels were smoother, which correspond more to the natural state of the alpine grassland distribution. These also agree with the accuracy assessment results at the landscape scale (Section 4.3), which demonstrated that at the landscape scale with more land cover types, hyperspectral imagery can provide more detailed information than multispectral imagery with the MESMA method.

5.2. RMSE Distribution

Because the whole area is situated high above sea level, in this study, we found a significant increase in the RMSE along with a variation in the elevation and slope form of the Landsat 8 OLI and Zhuhai-1 OHS imagery (Figure 6). This was particularly true in areas with strong topographic relief. We found a strong statistical relationship between the RMSE results from the Zhuhai-1 OHS ($R^2 = 0.98$) and Landsat 8 OLI imagery ($R^2 = 0.97$) and variations in the slope. The relationship between the RMSE results from the Zhuhai-1 OHS ($R^2 = 0.68$) and Landsat 8 OLI imagery ($R^2 = 0.74$) and the elevation change were also significant (Figure 6). This was consistent with previous spatial results (Section 4.2).

From this perspective, combined with our experience and results, we have confidence in saying that the variation in elevation and slope have a strong influence on the RMSE distribution, especially as measured by Zhuhai-1 OHS and Landsat 8 OLI imageries. However, previous studies have investigated factors influencing the accuracy of the DEM data (either SRTM DEM or ASTER GDEM [74–80]). These have reported that the main factors were topographic (slope angle and slope aspects) and vegetation (mainly forests). Szabó et al. [74] found that the DEM models had a significant bias compared to the same cross section of CLTIN, but the magnitude was greater in the forested area than the no-forested area. On gentle slopes, the deviation was smaller than on the steeper slopes, and ridges had larger vertical biases than valleys.

Slope aspects also had a significant effect on the accuracy. The SRTM models had the smallest bias on the south-facing slope, while for the ASTER GDEM, the western slopes were the most accurate. ASTER GDEM had an aspect dependency on easterly directions;

the slope and GDEM were positively related. Vegetation can alter the terrain height, which is challenging for the DEM accuracy and affects the RMSE results. However, it has also been shown that although the accuracy of DEM can be affected by topography, the errors were less than the dataset planned errors. These authors further suggested that the vegetation (mainly forests) also affects the accuracy of the DEM dataset [74]. However, in our study, forests are assent and the ground surface is mainly covered by alpine grassland and sparse shrubs. Therefore, the effects of vegetation to the accuracy of the DEM dataset were excluded and we consider that our DEM was able to meet the analytical requirements. Topographical correction is highly recommended when conducting research in a topographic relief region [9]. However, where there are differences in the image sources and terrain conditions, we also expect that future MESMA-based research in different landscapes could provide a better understanding of the RMSE distribution in broader data resources and locations.

Expect for the topography and DEM dataset itself which may affect the RMSE distribution, the other factor that impacts the RMSE distribution is the ground truth data we used during the unmixing procedure, because the ground truth data collection and framework design has a direct effect on the subsequent steps, such as image processing, classification, and result analysis [81]. In this study, the field data collected was used as a reference in the endmember selection stage, and the selected endmember was then used as the image unmixing sample, while the RMSE was generated during the image unmixing process. Therefore, from this perspective, the RMSE was affected by the field data used in this study. A previous study [82] has pointed out that the insufficient ground truth data may limit the accuracy result. Furthermore, the sample point distribution during the field data collection will also have an influence on the final result, such as being too close together between two sample points which will cause spatial auto-correlation, while too far apart in each point may lead to low representation. In addition, the location of the sample point is also an issue in field data collection; in the complex terrain area, if all the points are located in the flattened area, the mountain area will lack ground truth data and lead to a high error area, just like the RMSE distribution in our study. However, even though we have a high error area in the mountain part, we have no obvious evidence to conclude that the high error area was caused by a lack of ground truth datal; due to the high elevation in this region, we cannot reach to the mountain area to collect ground truth data, but in the future, a similar study that is conducted in the low altitude area may validate this.

6. Conclusions

This study explored the MESMA method to map the alpine grassland fraction coverage with the latest Zhuhai-1 OHS imagery. The results showed that the Zhuhai-1 OHS imagery can obtain a high image pixel unmixing percentage at both the pixel scale and landscape scale. The mean OA of the MESMA classification obtained at the pixel scale (96.5%) was significantly higher than that in the landscape scale (78.61%). Meanwhile, we observed different percentages of image pixel unmixed and accuracy for different image sources with the MESMA method under different model complexities. The overall conclusions from this study are (1) the Zhuhai-1 OHS in our research or hyperspectral imagery can provide a better performance to map both the pixel scale and landscape scale of vegetation in an area of interest; (2) Landsat 8 OLI or multispectral imagery can also meet the requirements of research work to discriminate vegetation and non-vegetation cover in the area of interest when combined with a suitable MESMA model complexity, such as the 3-EM model in this research; (3) from our analysis of the RMSE in the MESMA unmixing procedure, we have obtained apparent statistical evidence that reveals the relationship between RMSE and topographic relief. Hence, imagery terrain correction was highly recommended when conducting similar research in the region with rough terrains, such as in QTP and mountain areas.

In this study, we compared the ability of hyperspectral imagery (Zhuhai-1 OHS) and multispectral imagery (Landsat 8 OLI and Sentinel-2) to map the fraction coverage of

alpine grassland in the TRHR, and investigated the relationship between RMSE in the MESMA unmixing procedure and the topographic factors. The results acquired in this study can be used as the reference in making an alpine grassland conservation plan; the approaches and workflow to mapping the alpine grassland in this study can also be applied to help monitor grassland degradation in other grassland ecosystems. However, there are still some limitations in this study, such as that the acquisition date of Sentinel-2 images used in this study were about one month later than Zhuhai-1 OHS and Landsat 8 OLI, the accuracy of the DEM dataset used to analysis the RMSE distribution were also affected by topographic and vegetation factors, and the wavelength of the Zhuhai-1 OHS hyperspectral imagery used in this study were limited to 400–1000 nm; these limitations may have potentially impacted the accuracy of the results in our study. Therefore, in future work, more images that are in the same or closer time period can be used in the study, analysis of the DEM dataset accuracy can be performed prior to the application, and more advanced approaches such as deep learning could be applied to the grassland fraction coverage mapping.

Supplementary Materials: The following supporting information can be downloaded at: https://www.mdpi.com/article/10.3390/rs15092289/s1, Figure S1: Sample plot structure. 30 m by 30 m sample plot, the blue quadrats are nine 1 m by 1 m independent subplots set in four directions extending from the center of the sample plots; Figure S2: Comparison of unmixing results derived from Landsat 8 OLI, Sentinel-2, and Zhuhai-1 OHS images. (a) Full study area scene il-lustrating comparison locations a, b, c and d. Panel "c" is detail of area "c", and panel "d" is detail of area "d" where the top row is original imagery, and bottom row is unmixed imagery from indicated sources at the landscape scale. Red is the HCG fraction, green is the MCG fraction, and blue is the LCG fraction. The black area in the Zhuhai-1 OHS image was could masked. For detailed information for c and d see Figure S2; Figure S3: RMSE distribution of the three image sources. Digital Elevation Model (DEM) of the study region (a). RMSE from Landsat 8 OLI imagery (b). RMSE from Sentinel-2 imagery (c), and RMSE from Zhuhai-1 OHS imagery (d); Figure S4: RMSE distribution of the three image sources. Slope of the study region derived from the DEM (a). RMSE from Landsat 8 OLI imagery (b). RMSE from Sentinel-2 imagery (c), and RMSE from Zhuhai-1 OHS imagery (d); Figure S5: Distribution of RMSE observed from various aspect for Zhuhai-1 OHS, Sentinel-2, and Landsat 8 OLI imagery, respectively.

Author Contributions: F.X.: conceptualization, methodology, software, validation, writing original draft, funding acquisition. R.A.: conceptualization, review and editing, visualization, supervision, project administration, funding acquisition. X.G.: conceptualization, review and editing, supervision, project administration, funding acquisition. X.S.: conceptualization; writing—review and editing; supervision; project administration; funding acquisition. I.S.: methodology, review and editing, language editing. B.W.: methodology, resources, data curation, funding acquisition. Y.M.: review, comments, and editing. X.H.: review and comments. All authors have read and agreed to the published version of the manuscript.

Funding: This research was funded by the National Natural Science Foundation of China grant 41871326, the Natural Sciences and Engineering Research Council of Canada grant RGPIN- RGPIN-2022-04471, Key Project of Natural Science Research of Anhui Provincial Department of Education grant KJ2021A1083, and the China Scholarship Council grant 202106710115.

Data Availability Statement: Not applicable.

Acknowledgments: We sincerely thank the Zhuhai Orbita Aerospace Science and Technology Co., Ltd. (Orbita Aerospace) for generously providing the Zhuhai-1 OHS imagery. Additionally, we want to express our heartfelt gratitude to Zetian Ai, Meiru Zhu, Shengyin Zhao, Tong Jiang, and Yina Hu for their field data collection work.

Conflicts of Interest: The authors declare no conflict of interest.

References

1. An, R.; Zhang, C.; Sun, M.; Wang, H.; Shen, X.; Wang, B.; Xing, F.; Huang, X.; Fan, M. Monitoring grassland degradation and restoration using a novel climate use efficiency (NCUE) index in the Tibetan Plateau, China. *Ecol. Indic.* **2021**, *131*, 108208. https://doi.org/10.1016/j.ecolind.2021.108208.
2. Scurlock, J.M.O.; Hall, D.O. The global carbon sink: A grassland perspective. *Glob. Chang. Biol.* **1998**, *4*, 229–233. https://doi.org/10.1046/j.1365-2486.1998.00151.x.
3. Xu, D.; Guo, X.; Li, Z.; Yang, X.; Yin, H. Measuring the dead component of mixed grassland with Landsat imagery. *Remote Sens. Environ.* **2014**, *142*, 33–43. https://doi.org/10.1016/j.rse.2013.11.017.
4. Bardgett, R.D.; Bullock, J.M.; Lavorel, S.; Manning, P.; Schaffner, U.; Ostle, N.; Chomel, M.; Durigan, G.; Fry, E.L.; Johnson, D.; et al. Combatting global grassland degradation. *Nat. Rev. Earth Environ.* **2021**, *2*, 720–735. https://doi.org/10.1038/s43017-021-00207-2.
5. Piipponen, J.; Jalava, M.; de Leeuw, J.; Rizayeva, A.; Godde, C.; Herrero, M.; Kummu, M. Global assessment of grassland carrying capacities and relative stocking densities of livestock. *Glob. Chang. Biol.* **2022**, *28*, 3902–3919. https://doi.org/10.1002/essoar.10505875.1.
6. Török, P.; Brudvig, L.A.; Kollmann, J.; Price, J.; Tóthmérész, B. The present and future of grassland restoration. *Restor. Ecol.* **2021**, *29*, e13378. https://doi.org/10.1111/rec.13378.
7. Lehnert, L.W.; Meyer, H.; Wang, Y.; Miehe, G.; Thies, B.; Reudenbach, C.; Bendix, J. Retrieval of grassland plant coverage on the Tibetan Plateau based on a multi-scale, multi-sensor and multi-method approach. *Remote Sens. Environ.* **2015**, *164*, 197–207. https://doi.org/10.1016/j.rse.2015.04.020.
8. Piao, S.; Ciais, P.; Huang, Y.; Shen, Z.; Peng, S.; Li, J.; Zhou, L.; Liu, H.; Ma, Y.; Ding, Y.; et al. The impacts of climate change on water resources and agriculture in China. *Nature* **2010**, *467*, 43–51. https://doi.org/10.1038/nature09364.
9. Fassnacht, F.E.; Li, L.; Fritz, A. Mapping degraded grassland on the Eastern Tibetan Plateau with multi-temporal Landsat 8 data—Where do the severely degraded areas occur? *Int. J. Appl. Earth Obs. Geoinf.* **2015**, *42*, 115–127. https://doi.org/10.1016/j.jag.2015.06.005.
10. Wang, W.; Wang, Q.; Wang, H. The effect of land management on plant community composition, species diversity, and productivity of alpine Kobersia steppe meadow. *Ecol. Res.* **2005**, *21*, 181–187. https://doi.org/10.1007/s11284-005-0108-z.
11. Cao, J.; Adamowski, J.F.; Deo, R.C.; Xu, X.; Gong, Y.; Feng, Q. Grassland degradation on the Qinghai-Tibetan Plateau: Reevaluation of causative factors. *Rangel. Ecol. Manag.* **2019**, *72*, 988–995. https://doi.org/10.1016/j.rama.2019.06.001.
12. Li, C.; de Jong, R.; Schmid, B.; Wulf, H.; Schaepman, M.E. Changes in grassland cover and in its spatial heterogeneity indicate degradation on the Qinghai-Tibetan Plateau. *Ecol. Indic.* **2020**, *119*, 106641. https://doi.org/10.1016/j.ecolind.2020.106641.
13. Li, B. The rangeland degradation in North China and its preventive strategy. *Sci. Agric. Sin.* **1997**, *30*, 1–9.
14. Purevdorj, T.S.; Tateishi, R.; Ishiyama, T.; Honda, Y. Relationships between percent vegetation cover and vegetation indices. *Int. J. Remote Sens.* **1998**, *19*, 3519–3535. https://doi.org/10.1080/014311698213795.
15. Xing, F.; An, R.; Wang, B.; Miao, J.; Jiang, T.; Huang, X.; Hu, Y. Mapping the occurrence and spatial distribution of noxious weed species with multisource data in degraded grasslands in the Three-River Headwaters Region, China. *Sci. Total Environ.* **2021**, *801*, 149714. https://doi.org/10.1016/j.scitotenv.2021.149714.
16. Gao, Q.; Wan, Y.; Xu, H.; Li, Y.; Jiangcun, W.; Borjigidai, A. Alpine grassland degradation index and its response to recent climate variability in Northern Tibet, China. *Quat. Int.* **2010**, *226*, 143–150. https://doi.org/10.1016/j.quaint.2009.10.035.
17. Ge, J.; Meng, B.; Liang, T.; Feng, Q.; Gao, J.; Yang, S.; Huang, X.; Xie, H. Modeling alpine grassland cover based on MODIS data and support vector machine regression in the headwater region of the Huanghe River, China. *Remote Sens. Environ.* **2018**, *218*, 162–173. https://doi.org/10.1016/j.rse.2018.09.019.
18. Yagoub, H.; Belbachir, A.H.; Benabadji, N. Detection and mapping vegetation cover based on the Spectral Angle Mapper algorithm using NOAA AVHRR data. *Adv. Space Res.* **2014**, *53*, 1686–1693. https://doi.org/10.1016/j.asr.2014.03.020.
19. Dennison, P.E.; Qi, Y.; Meerdink, S.K.; Kokaly, R.F.; Thompson, D.R.; Daughtry, C.S.T.; Quemada, M.; Roberts, D.A.; Gader, P.D.; Wetherley, E.B.; et al. Comparison of methods for modeling fractional cover using simulated satellite hyperspectral imager spectra. *Remote Sens.* **2019**, *11*, 2072. https://doi.org/10.3390/rs11182072.
20. Tuia, D.; Verrelst, J.; Alonso, L.; Perez-Cruz, F.; Camps-Valls, G. Multioutput support vector regression for remote sensing biophysical parameter estimation. *IEEE Geosci. Remote Sens. Lett.* **2011**, *8*, 804–808. https://doi.org/10.1109/lgrs.2011.2109934.
21. Verrelst, J.; Muñoz, J.; Alonso, L.; Delegido, J.; Rivera, J.P.; Camps-Valls, G.; Moreno, J. Machine learning regression algorithms for biophysical parameter retrieval: Opportunities for Sentinel-2 and -3. *Remote Sens. Environ.* **2012**, *118*, 127–139. https://doi.org/10.1016/j.rse.2011.11.002.
22. Schwieder, M.; Leitao, P.J.; Suess, S.; Senf, C.; Hostert, P. Estimating fractional shrub cover using simulated EnMAP data: A comparison of three machine learning regression techniques. *Remote Sens.* **2014**, *6*, 3427–3445. https://doi.org/10.3390/rs6043427.
23. Fernandez-Manso, A.; Quintano, C.; Roberts, D.A. Burn severity influence on post-fire vegetation cover resilience from Landsat MESMA fraction images time series in Mediterranean forest ecosystems. *Remote Sens. Environ.* **2016**, *184*, 112–123. https://doi.org/10.1016/j.rse.2016.06.015.
24. Roberts, D.A.; Dennison, P.E.; Roth, K.L.; Dudley, K.; Hulley, G. Relationships between dominant plant species, fractional cover and Land Surface Temperature in a Mediterranean ecosystem. *Remote Sens. Environ.* **2015**, *167*, 152–167. https://doi.org/10.1016/j.rse.2015.01.026.

25. Roberts, D.A.; Gardner, M.; Church, R.; Ustin, S.; Scheer, G.; Green, R.O. Mapping chaparral in the Santa Monica Mountains using multiple endmember spectral mixture models. *Remote Sens. Environ.* **1998**, *65*, 267–279. https://doi.org/10.1016/S0034-4257(98)00037-6.
26. Wang, B.; An, R.; Zhang, Y.; Ai, Z. Mapping of Native Plant Species and Noxious Weeds in Typical Area of the Three-River Headwaters Region by Using Worldview-2 Imagery. In *Image and Graphics*; Springer: Berlin/Heidelberg, Germany, 2019; pp. 320–333. https://doi.org/10.1007/978-3-030-34113-8_27.
27. Wang, D.; Qiu, P.; Wan, B.; Cao, Z.; Zhang, Q. Mapping α- and β-diversity of mangrove forests with multispectral and hyperspectral images. *Remote Sens. Environ.* **2022**, *275*, 113021. https://doi.org/10.1016/j.rse.2022.113021.
28. Zhuhai Orbita Aerospace Science and Technology Co., Ltd.*"Zhuhai-1" Hyperspectral Satellite Data Products User Handbook_V2.5*; Zhuhai Orbita Aerospace Science and Technology Co., Ltd.: Zhuhai, China, 2021. (In Chinese)
29. Cao, L.; Zhang, D.; Guo, Q.; Zhan, J. Inversion of Water Quality Parameter bod5 Based on Hyperspectral Remotely Sensed Data in Qinghai Lake. In Proceedings of the 2021 IEEE International Geoscience and Remote Sensing Symposium IGARSS, Brussels, Belgium, 11–16 July 2021.
30. Mo, Y.; Zhong, R.F.; Cao, S.S. Orbita hyperspectral satellite image for land cover classification using random forest classifier. *J. Appl. Remote Sens.* **2021**, *15*, 014519. https://doi.org/10.1117/1.JRS.15.014519.
31. Fu, B.; Liu, M.; He, H.; Lan, F.; He, X.; Liu, L.; Huang, L.; Fan, D.; Zhao, M.; Jia, Z. Comparison of optimized object-based RF-DT algorithm and SegNet algorithm for classifying Karst wetland vegetation communities using ultra-high spatial resolution UAV data. *Int. J. Appl. Earth Obs. Geoinf.* **2021**, *104*, 102553. https://doi.org/10.1016/j.jag.2021.102553.
32. Wang, S.; Li, S.; Zheng, S.; Gao, W.; Zhang, Y.; Cao, B.; Cui, B.; Shao, D. Estimating biomass and carbon sequestration capacity of phragmites australis using remote sensing and growth dynamics modeling: a case study in Beijing hanshiqiao wetland nature reserve, China. *Sensors* **2022**, *22*, 3141. https://doi.org/10.3390/s22093141.
33. Kahaer, Y.; Tashpolat, N.; Shi, Q.; Liu, S. Possibility of Zhuhai-1 hyperspectral imagery for monitoring salinized soil moisture content using fractional order differentially optimized spectral indices. *Water* **2020**, *12*, 3360. https://doi.org/10.3390/w12123360.
34. Sheng, W.; Zhen, L.; Xiao, Y.; Hu, Y. Ecological and socioeconomic effects of ecological restoration in China's Three Rivers Source Region. *Sci. Total Environ.* **2019**, *650*, 2307–2313. https://doi.org/10.1016/j.scitotenv.2018.09.265.
35. Xiong, Q.; Xiao, Y.; Halmy, M.W.A.; Dakhil, M.A.; Liang, P.; Liu, C.; Zhang, L.; Pandey, B.; Pan, K.; El Kafraway, S.B.; et al. Monitoring the impact of climate change and human activities on grassland vegetation dynamics in the northeastern Qinghai-Tibet Plateau of China during 2000–2015. *J. Arid Land* **2019**, *11*, 637–651. https://doi.org/10.1007/s40333-019-0061-2.
36. Liu, J.; Xu, X.; Shao, Q. Grassland degradation in the "Three-River Headwaters" region, Qinghai Province. *J. Geogr. Sci.* **2008**, *18*, 259–273. https://doi.org/10.1007/s11442-008-0259-2.
37. Station, Q.R.W. *Grassland Resources of Qinghai*; Qinghai People's Publish Press Co., Ltd.: Xining, China, 2012.
38. Liya Wang, H.K. *Grassland Resources and the Dominated Plants Atlas of Sanjiangyuan Region*; Qinghai People's Publish Press: Xining, China, 2011.
39. Pan, D. *Study on the Types and Grade Partition Criterion of Black Soil Type Degraded Grassland in the Three-River Headwaters Region*; Gansu Agricultural University: Lanzhou, China, 2007.
40. Liu, J.; Xu, X.; Shao, Q. The spatial and temporal characteristics of grassland degradation in the Three-River Headwaters Region in Qinghai Province. *Acta Geogr. Scnica* **2008**, *63*, 364–376.
41. Dorji, T.; Totland, Ø.; Moe, S.R. Are droppings, distance from pastoralist camps, and Pika burrows good proxies for local grazing pressure? *Rangel. Ecol. Manag.* **2013**, *66*, 26–33. https://doi.org/10.2111/rem-d-12-00014.1.
42. Cliff, A.D.; Ord, J.K. *Spatial Autocorrelation*; Pion Limited: London, UK, 1973; p. 178.
43. Congalton, R.G. A review of assessing the accuracy of classification of remotely sensed data. *Remote Sens. Environ.* **1991**, *37*, 35–46. https://doi.org/10.1016/0034-4257(91)90048-B.
44. Congalton, R.G. Using spatial autocorrelation analysis to explore the errors in maps generated from remotely sensed data. *Photogramm. Eng. Remote Sens.* **1988**, *5*, 587–592.
45. Zhuhai Orbita Aerospace Science and Technology Co., Ltd. "*Zhuhai-1" OHS Hyperspectral Data Pre-Processing Handbook_V1.2*; Zhuhai Orbita Aerospace Science and Technology Co., Ltd.: Zhuhai, China, 2021. (In Chinese)
46. Gao, Y.; Zhang, W. A simple empirical topographic correction method for ETM+ imagery. *Int. J. Remote Sens.* **2009**, *30*, 2259–2275. https://doi.org/10.1080/01431160802549336.
47. Teillet, P.M.; Guindon, B.; Goodenough, D.G. On the slope-aspect correction of multispectral scanner data. *Can. J. Remote Sens.* **2014**, *8*, 84–106. https://doi.org/10.1080/07038992.1982.10855028.
48. Yao, M.; Huang, J.; Zhang, M.; Zhou, H.; Kuang, L.; Ye, F. A comprehensive evaluation method for topographic correction model of remote sensing image based on entropy weight method. *Open Geosci.* **2022**, *14*, 354–366. https://doi.org/10.1515/geo-2022-0359.
49. Xu, X.; Liu, J.; Zhang, S.; Li, R.; Yan, C.; Wu, S. *China's Multi-Period Land Use Land Cover Remote Sensing Monitoring Data Set (CNLUCC)*; Data Registration and Publishing System of Resource and Environmental Science Data Cloud Platform; Chinese Academy of Sciences: Beijing, China, 2018. Available online: http://www. resdc.cn (accessed on 20 July 2022).
50. Zanaga, D.; Van De Kerchove, R.; De Keersmaecker, W.; Souverijns, N.; Brockmann, C.; Quast, R.; Wevers, J.; Grosu, A.; Paccini, A.; Vergnaud, S.; et al. ESA WorldCover 10 m 2020 v100. 2021. Available online: https://zenodo.org/record/5571936#.ZEh4xM5ByUk (accessed on 16 February 2023).

51. ESA. WorldCover Product User Manual 1.0. European Space Agency. Available online: https://esa-worldcover.org/en (accessed on 16 February 2023).
52. Quintano, C.; Fernández-Manso, A.; Roberts, D.A. Enhanced burn severity estimation using fine resolution ET and MESMA fraction images with machine learning algorithm. *Remote Sens. Environ.* **2020**, *244*, 111815. https://doi.org/10.1016/j.rse.2020.111815.
53. Quintano, C.; Fernandez-Manso, A.; Roberts, D.A. Burn severity mapping from Landsat MESMA fraction images and Land Surface Temperature. *Remote Sens. Environ.* **2017**, *190*, 83–95. https://doi.org/10.1016/j.rse.2016.12.009.
54. Roberts, D.A.; Halligan, K.; Dennison, P.; Dudley, K.; Somers, B.; Crabbé, A. *VIPER Tools User Mannual Version 2.1*; UCSB VIPER LAB: Santa Barbara, CA, USA, 2019.
55. Dennison, P.E.; Roberts, D.A. The effects of vegetation phenology on endmember selection and species mapping in southern California chaparral. *Remote Sens. Environ.* **2003**, *87*, 295–309. https://doi.org/10.1016/j.rse.2003.07.001.
56. Dennison, P.E.; Halligan, K.Q.; Roberts, D.A. A comparison of error metrics and constraints for multiple endmember spectral mixture analysis and spectral angle mapper. *Remote Sens. Environ.* **2004**, *93*, 359–367. https://doi.org/10.1016/j.rse.2004.07.013.
57. Roberts, D.A.; Dennison, P.E.; Gardner, M.E.; Hetzel, Y.; Ustin, S.L.; Lee, C.T. Evaluation of the potential of hyperion for fire danger assessment by comparison to the airborne visible/infrared imaging spectrometer. *IEEE Trans. Geosci. Remote Sens.* **2003**, *41*, 1297–1310. https://doi.org/10.1109/tgrs.2003.812904.
58. Congalton, R.G.; Green, K. *Assessing the Accuracy of Remotely Sensed Data: Principles and Practices*, 3rd ed.; CRC Press: Boca Raton, FL, USA, 2019.
59. Quintano, C.; Fernández-Manso, A.; Roberts, D.A. Multiple Endmember Spectral Mixture Analysis (MESMA) to map burn severity levels from Landsat images in Mediterranean countries. *Remote Sens. Environ.* **2013**, *136*, 76–88. https://doi.org/10.1016/j.rse.2013.04.017.
60. Roth, K.L.; Roberts, D.A.; Dennison, P.E.; Alonzo, M.; Peterson, S.H.; Beland, M. Differentiating plant species within and across diverse ecosystems with imaging spectroscopy. *Remote Sens. Environ.* **2015**, *167*, 135–151. https://doi.org/10.1016/j.rse.2015.05.007.
61. Clark, M.L. Comparison of simulated hyperspectral HyspIRI and multispectral Landsat 8 and Sentinel-2 imagery for multi-seasonal, regional land-cover mapping. *Remote Sens. Environ.* **2017**, *200*, 311–325. https://doi.org/10.1016/j.rse.2017.08.028.
62. Ma, Z.; Redmond, R.L. Tau coefficients for accuracy assessment of classification of remote senisng data. *Photogramm. Eng. Remote Sens.* **1995**, *61*, 435–439.
63. Powell, R.; Roberts, D.; Dennison, P.; Hess, L. Sub-pixel mapping of urban land cover using multiple endmember spectral mixture analysis: Manaus, Brazil. *Remote Sens. Environ.* **2007**, *106*, 253–267. https://doi.org/10.1016/j.rse.2006.09.005.
64. Wang, J.J.; Zhang, Y.; Bussink, C. Unsupervised multiple endmember spectral mixture analysis-based detection of opium poppy fields from an EO-1 Hyperion image in Helmand, Afghanistan. *Sci. Total Environ.* **2014**, *476–477*, 1–6. https://doi.org/10.1016/j.scitotenv.2014.01.006.
65. Maselli, F. Multiclass spectral decomposition of remotely sensed scenes by selective pixel unmixing. *IEEE Trans. Geosci. Remote Sens.* **1998**, *36*, 1809–1820. https://doi.org/10.1109/36.718648.
66. Fernandez-Manso, A.; Quintano, C.; Roberts, D.A. Burn severity analysis in Mediterranean forests using maximum entropy model trained with EO-1 Hyperion and LiDAR data. *ISPRS J. Photogramm. Remote Sens.* **2019**, *155*, 102–118. https://doi.org/10.1016/j.isprsjprs.2019.07.003.
67. Franke, J.; Roberts, D.A.; Halligan, K.; Menz, G. Hierarchical Multiple Endmember Spectral Mixture Analysis (MESMA) of hyperspectral imagery for urban environments. *Remote Sens. Environ.* **2009**, *113*, 1712–1723. https://doi.org/10.1016/j.rse.2009.03.018.
68. Lewis, S.A.; Hudak, A.T.; Robichaud, P.R.; Morgan, P.; Satterberg, K.L.; Strand, E.K.; Smith, A.M.S.; Zamudio, J.A.; Lentile, L.B. Indicators of burn severity at extended temporal scales: A decade of ecosystem response in mixed-conifer forests of western Montana. *Int. J. Wildland Fire* **2017**, *26*, 755–771. https://doi.org/10.1071/wf17019.
69. Powell, R.L.; Roberts, D.A. Characterizing variability of the urban physical environment for a suite of cities in Rondônia, Brazil. *Earth Interact.* **2008**, *12*, 1–32. https://doi.org/10.1175/2008ei246.1.
70. Chen, F.; Wang, K.; Tang, T.F. Spectral unmixing using a sparse multiple-endmember spectral mixture model. *IEEE Trans. Geosci. Remote Sens.* **2016**, *54*, 5846–5861. https://doi.org/10.1109/tgrs.2016.2574331.
71. Okujeni, A.; van der Linden, S.; Tits, L.; Somers, B.; Hostert, P. Support vector regression and synthetically mixed training data for quantifying urban land cover. *Remote Sens. Environ.* **2013**, *137*, 184–197. https://doi.org/10.1016/j.rse.2013.06.007.
72. Brown, M.I.; Pearce, T.; Leon, J.; Sidle, R.; Wilson, R. Using remote sensing and traditional ecological knowledge (TEK) to understand mangrove change on the Maroochy River, Queensland, Australia. *Appl. Geogr.* **2018**, *94*, 71–83. https://doi.org/10.1016/j.apgeog.2018.03.006.
73. Ai, Z.T.; An, R.; Chen, Y.H.; Huang, L.J. Comparison of hyperspectral HJ-1A/HSI and multispectral Landsat 8 and Sentinel-2A imagery for estimating alpine grassland coverage in the Three-River Headwaters region. *J. Appl. Remote Sens.* **2019**, *13*, 014504. https://doi.org/10.1117/1.Jrs.13.014504.
74. Szabó, G.; Singh, S.K.; Szabó, S. Slope angle and aspect as influencing factors on the accuracy of the SRTM and the ASTER GDEM databases. *Phys. Chem. Earth Parts A/B/C* **2015**, *83–84*, 137–145. https://doi.org/10.1016/j.pce.2015.06.003.
75. Mukherjee, S.; Joshi, P.K.; Mukherjee, S.; Ghosh, A.; Garg, R.D.; Mukhopadhyay, A. Evaluation of vertical accuracy of open source Digital Elevation Model (DEM). *Int. J. Appl. Earth Obs. Geoinf.* **2013**, *21*, 205–217. https://doi.org/10.1016/j.jag.2012.09.004.

76. Tachikawa, T.; Kaku, M.; Iwasaki, A.; Gesch, D.B.; Oimoen, M.J.; Zhang, Z.; Danielson, J.J.; Krieger, T.; Curtis, B.; Haase, J.; et al. *ASTER Global Digital Elevation Model Version 2—Summary of Validation Results*; United States Geological Survey: Rishton, VA, USA, 2011; p. 27.
77. Farr, T.G.; Rosen, P.A.; Caro, E.; Crippen, R.; Duren, R.; Hensley, S.; Kobrick, M.; Paller, M.; Rodriguez, E.; Roth, L.; et al. The shuttle radar topography mission. *Rev. Geophys.* **2007**, *45*, 1-33. https://doi.org/10.1029/2005rg000183.
78. Rexer, M.; Hirt, C. Comparison of free high resolution digital elevation data sets (ASTER GDEM2, SRTM v2.1/v4.1) and validation against accurate heights from the Australian National Gravity Database. *Aust. J. Earth Sci.* **2014**, *61*, 213–226. https://doi.org/10.1080/08120099.2014.884983.
79. Forkuor, G.; Maathuis, B. *Comparison of SRTM and ASTER Derived Digital Elevation Models over Two Regions in Ghana-Implications for Hydrological and Environmental Modeling*; INTECH Open Access Publisher London: London, UK, 2012.
80. Carabajal, C.C.; Harding, D.J. ICESat validation of SRTM C-band digital elevation models. *Geophys. Res. Lett.* **2005**, *32*, 1-5. https://doi.org/10.1029/2005gl023957.
81. Pasolli, E.; Melgani, F.; Alajlan, N.; Conci, N. Optical image classification: A ground-truth design framework. *IEEE Trans. Geosci. Remote Sens.* **2012**, *51*, 3580–3597.
82. Li, S.; Hao, Q.; Gao, G.; Kang, X. The effect of ground truth on performance evaluation of hyperspectral image classification. *IEEE Trans. Geosci. Remote Sens.* **2018**, *56*, 7195–7206.